



Titanate nanofibers sensitized with ZnS and Ag₂S nanoparticles as novel photocatalysts for phenol removal

B. Barrocas, T.J. Entradas¹, C.D. Nunes, O.C. Monteiro*

Centro de Química e Bioquímica, Faculdade de Ciências, Universidade de Lisboa, Campo Grande, 1749-016 Lisboa, Portugal



ARTICLE INFO

Article history:

Received 27 March 2017
Received in revised form 27 June 2017
Accepted 29 June 2017
Available online 1 July 2017

Keywords:

Phenol photodegradation
Semiconductor nanocomposites
Ag₂S-ZnS sensitization
Titanate nanofibers

ABSTRACT

In this work, the synthesis of new nanocomposite materials, with enhanced optical and photocatalytic properties, was achieved through the combination of photoactive titanate nanofibers (TNF) with crystalline ZnS and Ag₂S nanoparticles. The TNF powders were obtained via hydrothermal synthesis and afterwards modified with the semiconductor nanoparticles. The Ag₂S and ZnS nanocrystallites were successfully grown onto the TNF surface, through a single-source precursor decomposition method, and ZnS-Ag₂S/TNF nanocomposite materials with distinct layouts were produced. After structural, morphological and optical characterization, the samples' photocatalytic performance to hydroxyl radical production was evaluated using terephthalic acid as probe molecule. The nanocomposite powders were investigated for phenol removal, while the identification and the time profiles of some by-products formed during the phenol degradation were carefully analysed.

Results suggest distinct photocatalytic pathways for the production of hydroxyl radical, as well as distinct phenol degradation mechanisms. The phenomenon was found to be dependent on the semiconductors layout. Ag₂S(ZnS/TNF) was the sample with the best photocatalytic activity, in terms of phenol removal and also considering the amount of by-products formed and time required for their degradation. Based on the photocatalytic degradation results, two energetic mechanisms for Ag₂S/TNF and Ag₂S(ZnS/TNF) performance were proposed and discussed.

© 2017 Elsevier B.V. All rights reserved.

1. Introduction

There has been an increasing interest in photo-assisted catalytic processes using nanocrystalline semiconductors as catalysts for the removal of persistent organic pollutants from wastewater systems [1]. Nevertheless, the complete mineralization of an organic pollutant with exclusive production of CO₂, H₂O and mineral acids, is not easy to be accomplished. In addition, the production of several by-products during irradiation, possibly more toxic than the initial pollutant should be carefully analysed.

Photocatalytic procedures are mostly based on the photo-generation of electron-holes pairs. These carriers are able to take part in oxidation/reduction reactions at the semiconductor surface, producing reactive radicals that will interact with the organic pollutants, leading to their progressive degradation and subsequently mineralization [2].

TiO₂ has been the mostly studied semiconductor for photocatalytic degradation applications. Nevertheless two limitations are recognized to it: the small percentage of sun radiation that possesses the required energy to produce photogenerated charge carriers and their high recombination rate, both limiting its use in large scale applications.

As a consequence, the development or improvement of active photocatalysts under visible light and the enhancement of charge separation are important aims to achieve in this research area. Among the prospective materials to be used in this perspective, titanate elongated nanostructures, including titanate nanofibers (TNF), can be very promising since they combine properties of conventional TiO₂ nanoparticles (e.g. photocatalytic activity) with the ion-exchangeable properties of layered titanates [3,4] and with high surface areas. Therefore, they have potentiality to be used in a wide range of applications, including catalysis [5,6] photocatalysis [7,8], nanomedicine [9,10], dye-sensitized solar cells [11], adsorbents [12], and sensors [13,14].

However, similarly to nanocrystalline TiO₂, titanate elongated nanostructures also present drawbacks regarding their application in photocatalysis: their high charge recombination rate and

* Corresponding author.

E-mail address: ocmonteiro@fc.ul.pt (O.C. Monteiro).

¹ Present address: Department of Chemistry, University of Liverpool, Crown Street, Liverpool L69 7ZD, United Kingdom.

wide bandgap (*ca.* 3.3 eV), limit drastically the electron-hole photo-generation under visible light irradiation.

The synergistic combination of two or more components, allows the enhancement of known photocatalytic materials with improved and/or innovated properties. The nanocomposite synthesis, combining two, e.g. $\text{TiO}_2/\text{Ag}_2\text{CrO}_4$ [15] or more components, e.g. $\text{ZnO}/\text{Ag}/\text{Ag}_2\text{WO}_4$ or $\text{Fe}_3\text{O}_4/\text{ZnO}/\text{CoWO}_4$ [16,17], has been one of the most popular methods to accomplish this goal. The combination of titanate elongated nanostructures with materials possessing activity in the visible range such as Bi_2S_3 [18] or Ag_2S , will extend the light absorption of the nanocomposite material to the visible region. At the same time, the photo-generated carriers recombination rate could be reduced by combining it, for instance, with nanocrystalline ZnS , a direct semiconductor with interesting optical properties [19].

Ag_2S is a direct low bandgap (\sim 1.0 eV) semiconductor that has not been truly investigated as single photocatalyst. However it was recently reported that under near-infrared irradiation, nanocrystalline Ag_2S particles demonstrated good photocatalytic performance and low recombination efficiency of the photogenerated electron–hole pairs in a photocatalytic process [20].

Conversely, nanocrystalline Ag_2S seems to be a good candidate for photosensitization of TiO_2 and TNF-based materials, since it absorbs radiation across the entire solar spectrum, with a large absorption coefficient. Moreover, the conduction and valence bands of Ag_2S are respectively, less anodic and more cathodic, than the ones of TiO_2 and TNF. Several experimental methods have been described to reach the incorporation of nanocrystalline Ag_2S on well-known photocatalysts, such as thermal decomposition [21], hydrothermal [22], in-situ solid-state process and subsequent cation-exchange reaction [23], and anodization, followed by successive ionic layer adsorption and reaction (SILAR) strategy [24].

Nanocrystalline ZnS is a direct semiconductor that shows interesting properties, and has been tested for several applications, including photocatalysis [25,26]. Despite the rapid generation of electron-hole pairs induced by photoexcitation, the use of single nanocrystalline ZnS is limited to the UV light irradiation due to its relatively wide bandgap (\sim 3.6 eV). The combination with other visible active materials, like Bi_2S_3 , may enhance the semiconductor photocatalytic properties which may lead to a better material for photocatalytic applications [18].

The successful combination of nanocrystalline Ag_2S and ZnS , for photocatalytic applications, has been reported as a double combination [27–29], or using different photoactive matrices, including TiO_2 nanoparticles and nanotubes [30], carbon nanotubes and fibers [23], POMs [31], and ZnO [32].

In this work, and aiming to design a new photocatalyst with enhanced light absorption (visible irradiation) and at the same time with lower rate of recombination of the photogenerated charge carriers, the combination of a wide and a narrow bandgap semiconductor in the same photocatalytic material was assessed. Here, the production of TNF-based nanocomposite crystalline materials by the combination of photocatalytic active titanate nanofibers with crystalline Ag_2S and ZnS nanoparticles is, for the first time, described. In a first stage and through the Ag_2S sensitization, an enlargement of the TNF optical absorption, through the entire visible spectrum range, was observed. By adding ZnS nanoparticles to the $\text{Ag}_2\text{S}/\text{TNF}$, and considering the optical behaviour described for this semiconductor, the reduction of the photogenerated charge carriers was aimed.

Distinct layout combinations of Ag_2S and ZnS crystallites on the TNF surface were tested and the results indicate that the final nanocomposite properties are dependent on them. The possibility of using these materials for pollutant removal, mainly for phenol photocatalytic degradation was studied and the secondary prod-

ucts identified. A mechanism for these nanocomposites catalytic activity was proposed and discussed.

2. Materials and methods

All reagents (analytical grade) were used as received, without any purification. The solutions were prepared using distilled water.

2.1. Experimental

2.1.1. TNF synthesis

The titanate nanofibers were obtained via a method described in the literature [33]. A titanium solution was prepared by a 1:2 dilution of 50 mL of TiCl_3 (10 wt.% in 20–30 wt.% HCl) in a 2 M of aqueous HCl. A 4 M NH_4OH aqueous solution was then added drop-wise to the TiCl_3 solution, under vigorous stirring, until the precipitation of a white solid, the precursor for the TNF synthesis. The resulting suspension was kept overnight at room temperature. After that, the powder was washed several times with water, filtered and stored.

The TNF particles were obtained using \sim 6 g of the precursor in *ca.* 60 mL of NaOH 10 M solution in an autoclave system at 200 °C, during 12 h. After cooling to room temperature, the suspension was filtered and the solid washed several times with water.

2.1.2. ZnS precursor synthesis

Zinc diethyldithiocarbamate, $\{\text{Zn}[\text{S}_2\text{CN}(\text{C}_2\text{H}_5)_2]_2\}$, was prepared as reported earlier [34]: 20 mmol of ethylenediamine ($\text{C}_2\text{H}_8\text{N}_2$) and 13.5 mmol of carbon disulphide (CS_2) were added to a suspension containing 10 mmol of ZnCl_2 in water (50 mL). The mixture was stirred over 2 h and a white solid was obtained. The solid was recrystallized from hot chloroform or dichloromethane.

2.1.3. TNF sensitization with nanocrystalline Ag_2S and ZnS

The $\text{Ag}_2\text{S}/\text{TNF}$ and ZnS/TNF samples were prepared based on a procedure reported previously [29]. The ZnS/TNF and $\text{Ag}_2\text{S}/\text{TNF}$ samples were prepared using the standard procedure described below; $\{\text{Zn}[\text{S}_2\text{CN}(\text{C}_2\text{H}_5)_2]_2\}$ (previously prepared, Section 2.1.2) and commercial $\{\text{Ag}_2[\text{S}_2\text{CN}(\text{C}_2\text{H}_5)_2]_2\}$ were used as ZnS and Ag_2S precursors, respectively.

2.1.3.1. Standard procedure. TNF were modified with MS (metal sulphide) by adding 2.5 mL of ethylenediamine to 50 mL of an acetone suspension containing 0.125 mmol of MS organometallic precursor and 0.250 g of TNF powder. The suspension was stirred at reflux temperature, during 4 h. After cooling to room temperature, the obtained solid was isolated by centrifugation, washed with acetone and dried at room temperature.

The ZnS/TNF (beige solid) and $\text{Ag}_2\text{S}/\text{TNF}$ (dark grey solid) could be used afterwards to prepare the composite samples.

The co-sensitized nanocomposite samples were obtained as follows:

- i) $\text{Ag}_2\text{S}(\text{ZnS}/\text{TNF})$: after preparing, using the standard procedure, and dried, the ZnS/TNF powder was used with $\{\text{Ag}_2[\text{S}_2\text{CN}(\text{C}_2\text{H}_5)_2]_2\}$ in acetone:ethylenediamine mixture (standard procedure) for the Ag_2S nanoparticles growth;
- ii) $\text{ZnS}(\text{Ag}_2\text{S}/\text{TNF})$: this sample was obtained using the standard procedure and $\{\text{Ag}_2[\text{S}_2\text{CN}(\text{C}_2\text{H}_5)_2]_2\}$ as Ag_2S precursor. After dried, the powder was modified using the same procedure again but $\{\text{Zn}[\text{S}_2\text{CN}(\text{C}_2\text{H}_5)_2]_2\}$ as ZnS precursor.
- iii) $\text{Ag}_2\text{S}(\text{ZnS}/\text{TNF})$: this sample was prepared using the standard procedure, using at same time both metal sulphide precursors, $\{\text{Ag}_2[\text{S}_2\text{CN}(\text{C}_2\text{H}_5)_2]_2\}$ and $\{\text{Zn}[\text{S}_2\text{CN}(\text{C}_2\text{H}_5)_2]_2\}$.

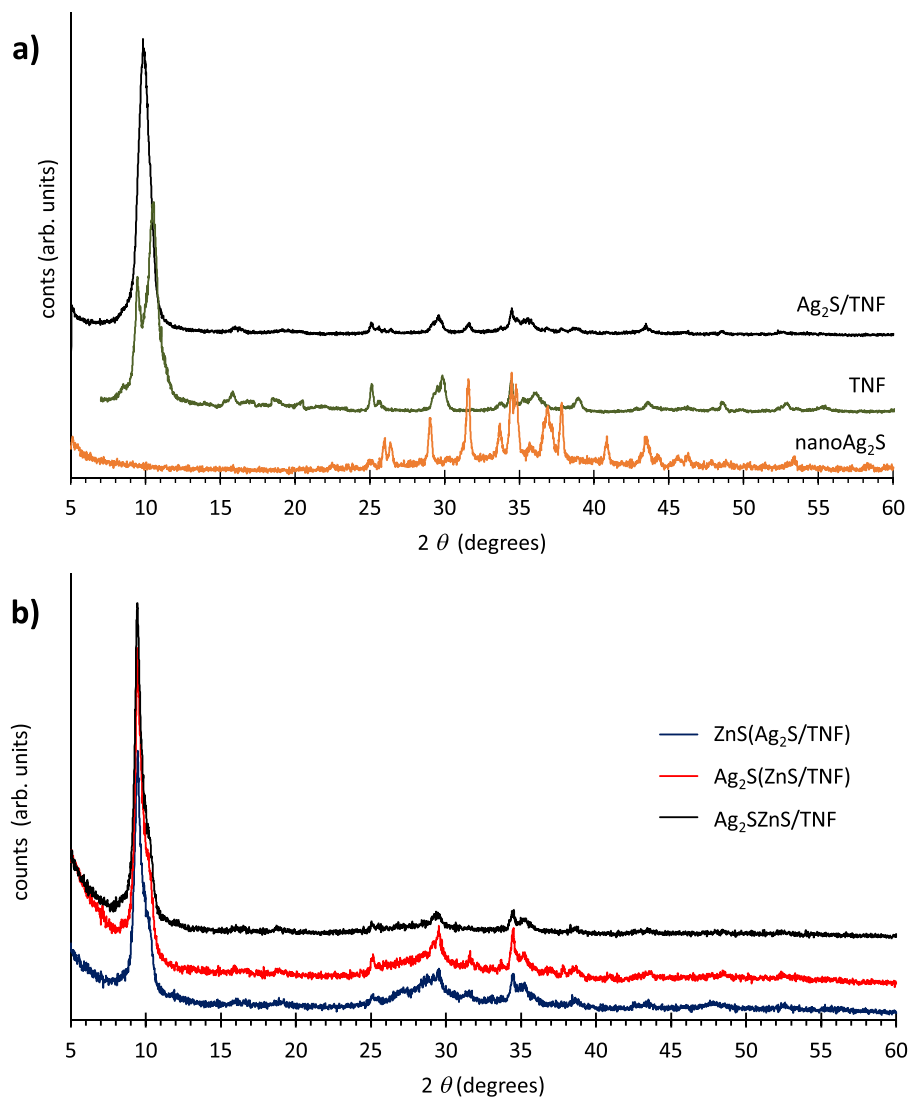


Fig. 1. a) XRD patterns for TNF, Ag₂S/TNF, and nanoAg₂S prepared samples; b) XRD patterns of the Ag₂S-ZnS/TNF, Ag₂S(ZnS/TNF), and ZnS(Ag₂S/TNF) samples.

2.1.4. ZnS and Ag₂S crystalline nanoparticles synthesis

Samples of crystalline ZnS, Ag₂S and Ag₂S-ZnS nanoparticles were prepared as described in Section 2.1.3 (standard procedure), but in the absence of TNF particles. Following the same nomenclature used for the co-sensitized TNF samples, these powders were labelled as nanoZnS(Ag₂S), nanoAg₂S(ZnS) and nano(Ag₂S/ZnS).

2.2. Photodegradation experiments

All photodegradation experiments were conducted using a refrigerated photoreactor [32]. A 450W Hanovia medium-pressure mercury-vapour lamp was used as radiation source, the total irradiated energy being 40–48% in the ultraviolet range and 40–43% in the visible range. Prior to irradiation, the suspensions were stirred in darkness conditions during 60 min to ensure the adsorption equilibrium.

Terephthalic acid (TA) was used as probe molecule to evaluate the hydroxyl radical production. In this reaction, the OH[•] radical, formed during catalyst irradiation, converts the terephthalic acid into 2-hydroxyterephthalic acid (HTA), a product easily quantified by fluorescence spectroscopy. For the photocatalytic experiments, 150 mL of a TA solution (3 mM, in 0.01 M NaOH) and 10 mg of each powder were used.

For phenol photocatalytic experiments, suspensions were obtained by adding 25 mg of the powder to 150 mL of a phenol aqueous solution (20 ppm). During irradiation, suspensions were sampled at regular intervals, centrifuged and analysed by GC-MS.

2.3. Characterization techniques

X-ray powder diffraction was performed using a Philips X-ray diffractometer (PW 1730) with automatic data acquisition (APD Philips v3.6B), using Cu K α radiation ($\lambda = 0.15406$ nm) and working at 40 kV/30 mA. The diffraction patterns were collected in the 2θ range of 5°–60° with a 0.02° step size and an acquisition time of 200 s per step. Transmission electron microscopy (TEM) and selected area electron diffraction (SAED) were carried out on a JEOL 200CX microscope operating at 200 kV. The elemental qualitative analyses of the samples were performed by energy dispersive X-ray spectroscopy (EDS). The diffuse reflectance spectra (DRS) of the powders were recorded using a UV-vis absorption spectrophotometer (Shimadzu, UV-2600PC) with an ISR 2600plus integration sphere, in the 220–1400 nm wavelength range.

Specific surface areas were obtained by the B.E.T. method, from nitrogen (AirLiquide, 99.999%) adsorption data at -196°C , using a volumetric apparatus from Quantachrome mod NOVA 2200e. The

samples, weighing approximately 55 mg, were previously degassed for 2.5 h at 150 °C at a pressure lower than 0.133 Pa.

During photocatalytic experiments, the phenol solutions were monitored using a GC-MS; the conversion of products were monitored by taking samples and analyzing them using a Shimadzu QP2100-Plus GC/MS system with a Tecknokroma TRB-5MS capillary column. A Spex Fluorolog 3-22/Tau 3 was used to record the fluorescence spectra of 2-hydroxyterephthalic acid (excitation and emission wavelengths 315 and 425 nm, respectively) and for the powders photoluminescence (PL) spectra (excitation at 286 nm).

3. Results and discussion

3.1. $\text{Ag}_2\text{S}/\text{TNF}$ samples

3.1.1. Crystalline structure and morphology

XRD patterns for TNF, $\text{Ag}_2\text{S}/\text{TNF}$, and nano Ag_2S prepared samples are shown in Fig. 1a. The $\text{Ag}_2\text{S}/\text{TNF}$ diffraction pattern evidences a peak at $2\theta \sim 10^\circ$, which corresponds to the interlayer distance between the TiO_6 layers of the typical TNF crystalline structure, as described previously [13]. No shifts in this peak were observed indicating that the sensitization doesn't damage the TNF crystalline structure. The presence of crystalline Ag_2S acanthite (JCPDS Card File: 00-014-0072) over the TNF surface can be confirmed through a comparative analysis of the XRD patterns of the $\text{Ag}_2\text{S}/\text{TNF}$ and nano Ag_2S samples. The ZnS/TNF and nano ZnS samples were also characterized by XRD (results not shown) and the results agree with the ones previously reported [35].

The samples obtained through the co-sensitization process were also characterized by XRD and the patterns of the $\text{Ag}_2\text{S}\text{ZnS}/\text{TNF}$ (TNF sensitized simultaneously with nanocrystalline ZnS and Ag_2S), $\text{Ag}_2\text{S}(\text{ZnS}/\text{TNF})$ (ZnS/TNF sensitized with Ag_2S) and $\text{ZnS}(\text{Ag}_2\text{S}/\text{TNF})$ ($\text{Ag}_2\text{S}/\text{TNF}$ sensitized with ZnS) samples are present in Fig. 1b. As can be seen, all the three co-sensitized samples show similar XRD patterns; from those the presence of nanocrystalline ZnS and Ag_2S can be concluded.

The morphology of the $\text{Ag}_2\text{S}/\text{TNF}$, ZnS/TNF , nano Ag_2S and nano ZnS samples was analysed by transmission electronic microscopy and some images are shown in Fig. 2. Prior to sensitization, the TNF powder is morphologically homogeneous and consists of elongated nanoparticles like fibers (Fig. 2a) [14]. Fig. 2b and c shows TEM images of the $\text{Ag}_2\text{S}/\text{TNF}$ and ZnS/TNF nanocomposite samples, respectively. The presence of small spheroidal nanoparticles spread over the TNF surface, after Ag_2S sensitization, is visible in the $\text{Ag}_2\text{S}/\text{TNF}$ sample, contrasting with the TNF surface completely covered by extremely small ZnS nanocrystallites, visible in the ZnS/TNF sample. These two morphologies are similar to those obtained for the nano Ag_2S and nano ZnS samples, suggesting no influence of the TNF on the second semiconductor growth process (images not shown).

The morphology of the co-sensitized samples was also analyzed by TEM and the images of $\text{Ag}_2\text{S}\text{ZnS}/\text{TNF}$, $\text{ZnS}(\text{Ag}_2\text{S}/\text{TNF})$ and $\text{Ag}_2\text{S}(\text{ZnS}/\text{TNF})$ samples are shown in Fig. 3. Images of the nano $\text{Ag}_2\text{S}\text{ZnS}$, nano($\text{ZnS}/\text{Ag}_2\text{S}$) and nano($\text{Ag}_2\text{S}/\text{ZnS}$) samples, prepared without TNF, were also included in Fig. 3 to allow comparisons. As can be seen, all the sensitized TNF samples exhibit identical morphology: the existence of a second-layer covering the TNF surface is clearly seen indicating the presence of nanocrystalline ZnS and Ag_2S particles. On the other hand, it was more difficult to identify the Ag_2S nanoparticles for the samples prepared using a stepwise process, $\text{ZnS}(\text{Ag}_2\text{S}/\text{TNF})$ and $\text{Ag}_2\text{S}(\text{ZnS}/\text{TNF})$, than for the sample obtained through the one-pot approach ($\text{Ag}_2\text{S}\text{ZnS}/\text{TNF}$).

EDS analyses were performed over the TNF modified samples, indicating the presence of Ag and/or Zn and S elements, together

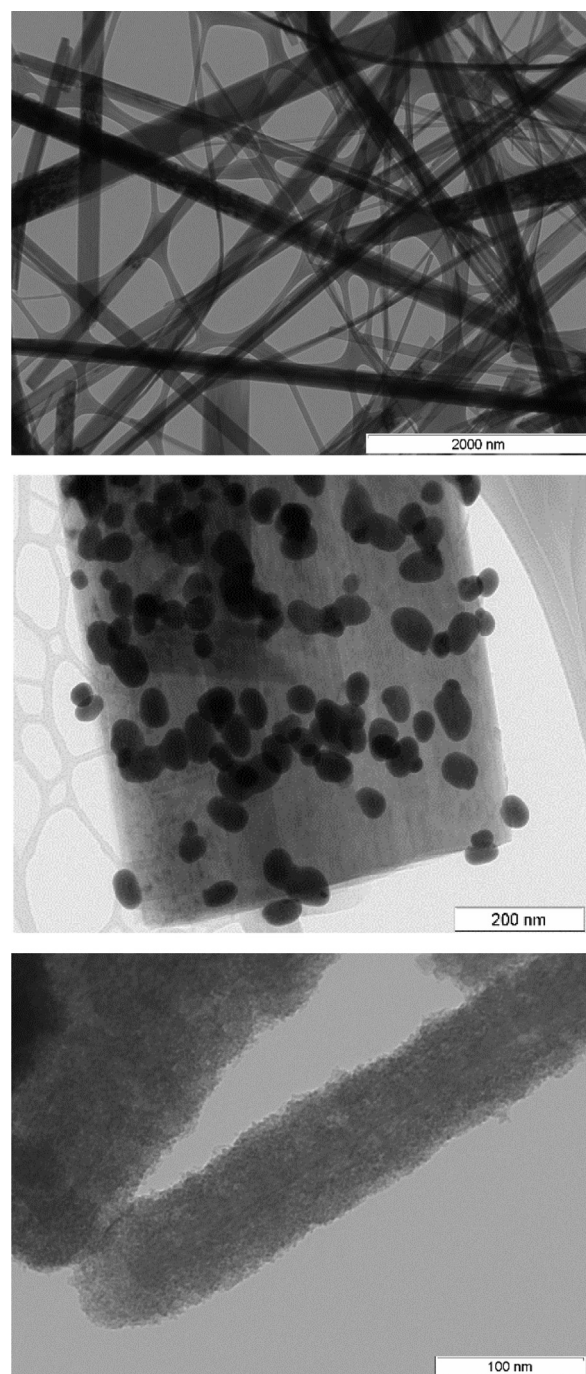


Fig. 2. TEM images of a) TNF, b) $\text{Ag}_2\text{S}/\text{TNF}$, and c) ZnS/TNF samples.

with Ti and Na from the TNF matrix (Fig. S1, Supplementary Information). The EDS mapping of the $\text{Ag}_2\text{S}(\text{ZnS}/\text{TNF})$ sample was also performed (Fig. S2) to assess the distribution of the elements. An uniform distribution was visualized for all the elements, including Na, Ti, S, Zn and Ag, suggesting the existence of excellent interface contacts between TNF, Ag_2S and ZnS nanoparticles.

The surface area of the prepared samples was evaluated using the B.E.T. methodology. As expected, slight changes were observed on the TNF surface area ($50.4 \text{ m}^2 \text{ g}^{-1}$) after modification with ZnS and Ag_2S nanoparticles. However, no relation between the nanocomposite layout and surface area increase was possible to be established. The values obtained for the nanocomposite powders

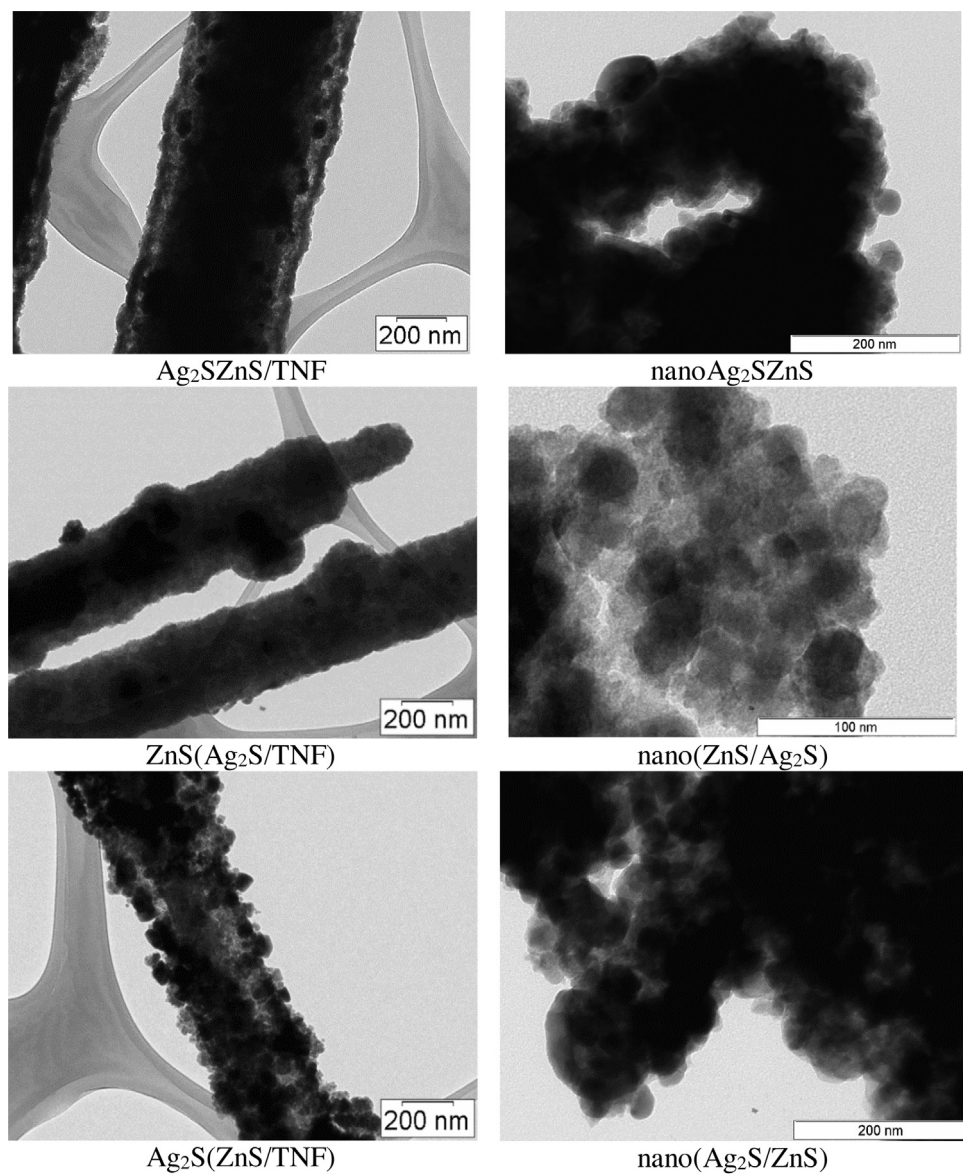


Fig. 3. TEM images of the Ag_2S -ZnS nanocomposite samples prepared with and without the presence of TNF.

surface areas were 53.1, 55.0 and $55.6 \text{ m}^2 \text{ g}^{-1}$ for the $\text{Ag}_2\text{SZNs/TNF}$, $\text{ZnS}(\text{Ag}_2\text{S/TNF})$ and $\text{Ag}_2\text{S}(\text{ZnS/TNF})$ samples, respectively.

3.1.2. Optical characterization

The effect of the Ag_2S and ZnS sensitization on pristine TNF optical properties was evaluated by recording the diffuse reflectance (R) spectra. R is related with the Kubelka-Munk absorption function, F_{KM} , by the relation $F_{KM}(R) = (1 - R)^2/2R$, which is proportional to the absorption coefficient [36].

The absorption spectrum of the TNF sample prior to sensitization (Fig. 4) shows an absorption band edge at 350 nm that corresponds to an energy bandgap (E_g) of 3.33 eV. After sensitization with Ag_2S nanoparticles, this optical feature is extended and a new band edge near 1200 nm is observed. This effect is mainly justified due to the Ag_2S particles' absorption, ($E_g = 0.90\text{--}1.05 \text{ eV}$). E_g values of 0.89 eV and 0.85 eV were estimated for nanoAg_2S and $\text{Ag}_2\text{S/TNF}$ samples, respectively.

The absorption behaviour of the three co-sensitized samples (not shown) is very similar to the one of $\text{Ag}_2\text{S/TNF}$ reported in Fig. 4-inset, with all the samples absorbing in the entire visible spectrum range. The presence of nanocrystalline Ag_2S particles overlaps the

Table 1
Bandgap energies calculated for the co-sensitized samples.

Sample ID	E_g (eV)
TNF	3.33
$\text{Ag}_2\text{S/TNF}$	0.85
nanoAg_2S	0.89
$\text{Ag}_2\text{S}(\text{ZnS/TNF})$	0.98
$\text{ZnS}(\text{Ag}_2\text{S/TNF})$	0.99
$\text{Ag}_2\text{SZNs/TNF}$	0.85

optical signals from both TNF and ZnS nanoparticles. According to TEM images, this effect was expected once this semiconductor has a typical absorption edge very close to (or even lower than) TNF [35].

Furthermore, since the absorption of the three co-sensitized samples is dominated by the presence of the nanocrystalline Ag_2S , the three absorption band edges are close to the value obtained for the nanoAg_2S sample. The bandgap energy for the $\text{Ag}_2\text{SZNs/TNF}$, $\text{ZnS}(\text{Ag}_2\text{S/TNF})$ and $\text{Ag}_2\text{SZNs/TNF}$ samples were calculated and are present in Table 1. No significant differences were observed between the supported and unsupported semiconductor systems.

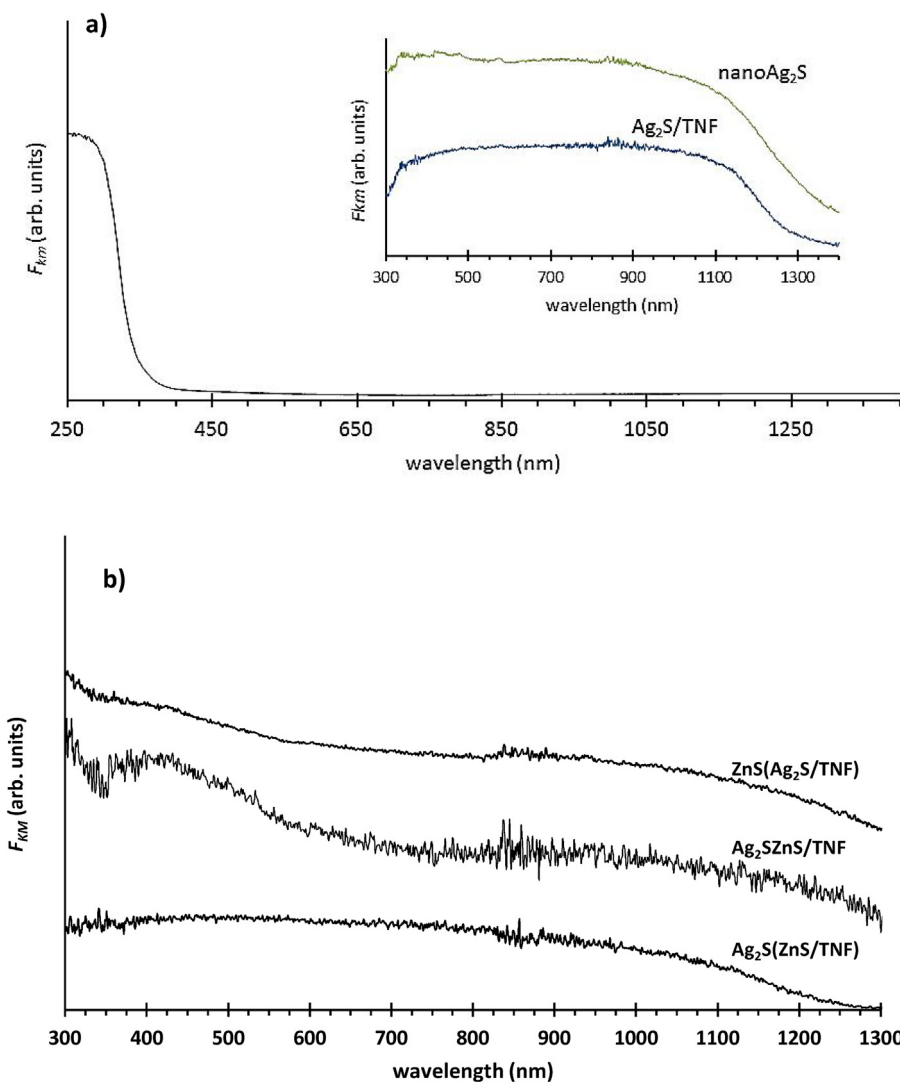
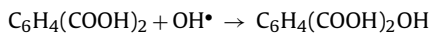


Fig. 4. a) Optical absorption spectra of the TNF sample. Inset: optical spectra of the nanoAg₂S and Ag₂S/TNF prepared powders; b) optical spectra of the ZnS(Ag₂S/TNF), Ag₂SZnS/TNF and Ag₂S(ZnS/TNF) samples.

3.2. Hydroxyl radical photocatalytic production evaluation

The feasibility of the prepared nanocomposite materials for future photocatalytic applications was investigated through the evaluation of the photocatalytic production of hydroxyl radical (OH[•]). The evaluation of the hydroxyl radical production was performed using terephthalic acid (TA), an OH[•] scavenger, which does not react with other radicals, such as O₂[−] or H₂O₂. The OH[•] radical can convert terephthalic acid into the fluorescent 2-hydroxyterephthalic acid (HTA) through the reaction:



All synthesised co-sensitised materials along with nanoAg₂S, Ag₂S/TNF and TNF samples were tested for the TA photocatalytic degradation. Fig. 5a shows the HTA production regarding the Ag₂S/TNF related samples for a period of 20 min of irradiation. All the samples have demonstrated to be photocatalytic active for this reaction, with the highest HTA generation, corresponding to the highest OH[•] formation, being achieved using the nanoAg₂S sample as catalyst. For the same period, identical photocatalytic performances were attained with TNF and Ag₂S/TNF samples.

A closer look at the results showed an intriguing result: if Ag₂S was catalytically active for the hydroxyl radical production, the use

of Ag₂S/TNF could have resulted in an enhancement of the pristine TNF catalytic performance. On the other hand, there are some reports attesting that the direct production of this oxidant species is not expectable through Ag₂S irradiation [20], due to its bandgap and valence band (VB) energies and the extremely high hydroxyl radical redox potential (2.33 eV) [37].

To better understand the mechanism in charge for this catalytic behaviour, the conduction and valence bands (CB and VB, respectively) potentials for nanoAg₂S were calculated.

The VB potential (E_{VB}) can be determined by the equation [38]:

$$E_{VB} = X - E^e + 0.5E_g \quad (1)$$

where X is the Pearson absolute electronegativity of the semiconductor [39], which is defined as the geometric mean of the absolute electronegativity of the constituent atoms, E^e is the energy of free electrons on the hydrogen scale (ca. 4.5 eV), and E_g is the bandgap of the semiconductor.

The conduction band (CB) potential can be determined by:

$$E_{CB} = E_{VB} - E_g \quad (2)$$

The value of X for Ag₂S is 4.96 eV [35] and the top of the VB and the bottom of the CB for the nanocrystalline Ag₂S sample were calculated and values of 0.905 and 0.015 eV were obtained,

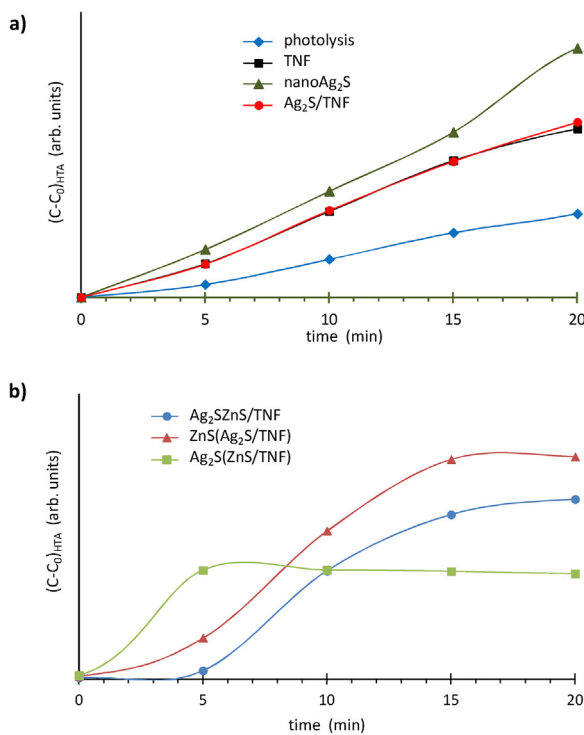


Fig. 5. HTA concentration variation during 20 min of irradiation of a TA solution (3 mM, 150 mL) using 10 mg of TNF and Ag₂S modified photocatalysts (a) and using the co-sensitized samples (b).

respectively. These values agree with several published works and confirm the impossibility of hydroxyl radical formation via H₂O photo-oxidation [38] and also of superoxide radical directly from molecular oxygen [40,41]. However, a two steps mechanism for hydroxyl radical formation, is proposed: the production of H₂O₂ from molecular O₂ (~0.68 V) and subsequently the H₂O₂ \rightarrow OH[•] (~0.38 V) reduction reaction (Fig. 6). The experimental results obtained are in agreement with this proposed mechanism.

On the other hand, identical results obtained with the TNF and Ag₂S/TNF, which were inferior than the ones obtained with the nanoAg₂S sample, could be explained by a combination of several

factors: despite the fact that TNF sample is able by itself to produce hydroxyl radical through photogenerated holes reaction, the Ag₂S presence over the TNF surface absorbs part of the radiation which contribute for the reduction of OH[•] production; in the CB, the electrons will be able to reduce O₂ to O₂[•] and H₂O₂, but the amount of Ag₂S present in both samples (nanoAg₂S and Ag₂S/TNF) was dramatically different, being higher for the nanoAg₂S sample.

Despite the higher OH[•] generation, a practical application of nanocrystalline Ag₂S as photocatalyst is not attractive. The synthetic costs, unfriendly scale-up to an industrial level as well as the tiny amount of powder produced per batch and the difficult solid-solution separation after photocatalysis kills the applicability of this material for photocatalytic purposes. It should be note that for the same quantity of photocatalyst, the amount of photoactive Ag₂S present in the nanocomposite Ag₂S/TNF sample was much lower than the one present in the nanoAg₂S sample. Furthermore, the composite solid recovery, after the photocatalytic experiments, was easier since the particles were larger, making this material more attractive for future applications. These seemed to be good reasons to support the use of the Ag₂S/TNF nanocomposite instead of the crystalline Ag₂S nanoparticles.

To check if nanocrystalline ZnS could have a positive effect in this process, the hydroxyl radical production was evaluated in the presence of the co-photosensitized samples and the results are shown in Fig. 5b. After 20 min of irradiation the highest OH[•] production was attained using the ZnS(Ag₂S/TNF) sample and the lower photocatalytic performance was observed using the Ag₂S(ZnS/TNF) powder; in this last case with an HTA amount similar to that produced during photolysis. It was interesting that the production of HTA over the radiation time was not continuous and a quasi-equilibrium state was attained after a certain period of irradiation. This result suggested that Ag₂S does not follow the same mechanistic pathway for the generation of the hydroxyl radical. Furthermore, it was not clear that the Ag₂S nanoparticles irradiation would quench and limit the photoactivity of the ZnS/TNF module as shown in Fig. 5b.

For instance, using the Ag₂S(ZnS/TNF) sample, the production of HTA increased rapidly up to 5 min and retained this level for longer irradiation times. However, and although this situation was the faster one, it was also the one corresponding to a smaller quantity of HTA produced, when compared to the use of ZnS(Ag₂S/TNF) or Ag₂SZnS/TNF samples.

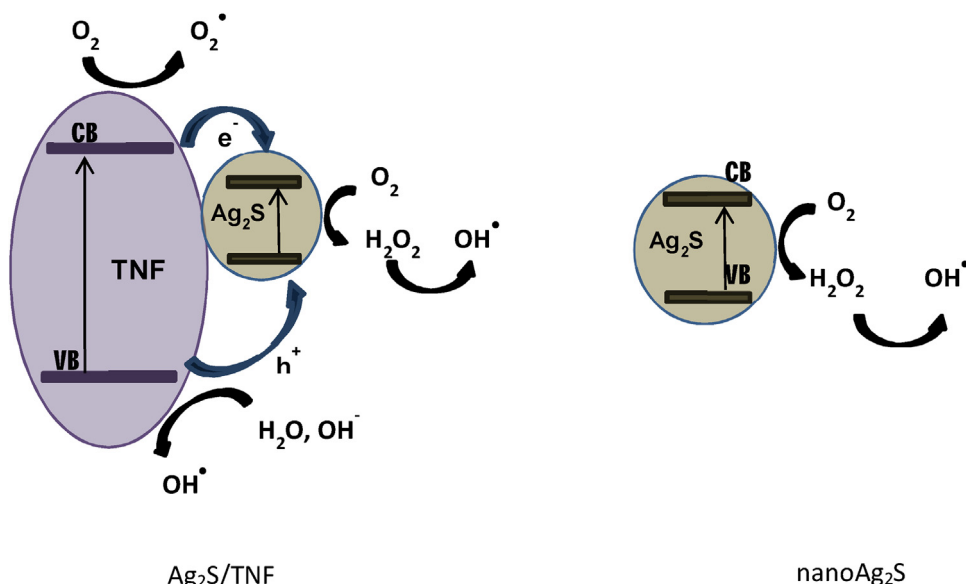


Fig. 6. Proposed band structure scheme for Ag₂S/TNF and nanoAg₂S particles and mechanism of photo-induced oxidant radical formation.

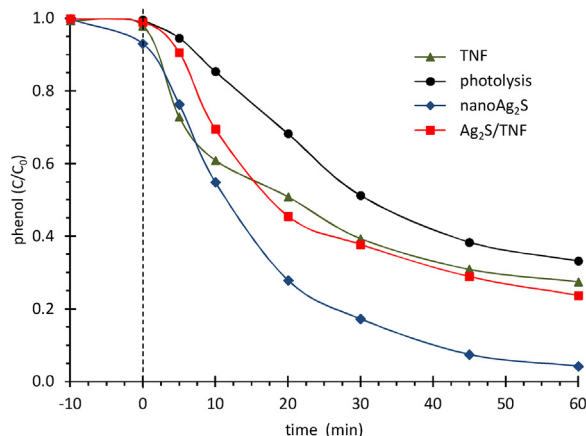


Fig. 7. Phenol photocatalytic degradation of a 20 ppm aqueous solution during 60 min of irradiation using the prepared samples as photocatalysts (0.16 g/L).

3.3. Phenol photocatalytic degradation

The most promising materials, Ag₂S/TNF and the co-sensitized samples were irradiated and the phenol photodegradation evaluated. Prior to photo-irradiation, the samples' ability for phenol adsorption was evaluated and less than 7% of the initial phenol was adsorbed after 1 h of contact in dark conditions.

3.3.1. Using TNF and Ag₂S/TNF

To better understand the effect of sensitization on the photocatalytic activity of TNF, the phenol photodegradation was first studied using the pristine and the Ag₂S/TNF modified sample. Fig. 7 shows the time profiles of phenol degradation during 60 min of irradiation, for the photolysis (no catalyst) and using TNF, nanoAg₂S,

and Ag₂S/TNF as catalysts. As can be seen, after 60 min of irradiation, both samples, TNF and Ag₂S/TNF demonstrated similar photocatalytic activity for this process with 73% and 76% of the initial phenol degraded, respectively. Without any catalyst and for the same irradiation period only 67% of the pollutant was removed. For comparison, the nanoAg₂S sample was also used as photocatalyst and the results indicated that this was the best performer of this set of three samples, with 96% of phenol degradation for the same period of time.

However, it must be re-stated that this sample has the highest production cost and for this reason the nanoAg₂S sample was not considered in further studies.

The catalytic performances of TNF and Ag₂S/TNF samples were found to be similar, although different degradation by-products were identified by GC-MS, including benzoquinone, hydroquinone, resorcinol and catechol (Fig. 8). This was an evidence of distinct degradation pathways justifying an active role of the Ag₂S nanoparticles at the TNF surface.

A close analysis of Fig. 8a allowed concluding that the photocatalysed degradation processes follow different reaction mechanisms, distinct from those of photolysis. Furthermore it presents different degradation by-products and/or removal time profiles.

After 60 min, the main by-product (71%) for the TNF catalysis process was an alcoholic mixture of catechol and resorcinol, with 14–15% of benzoquinone and also of hydroquinone. For the photolysis, this mixture was also the main component but representing only 50% of the by-products produced, being hydroquinone and benzoquinone with 33% and 17% conversion, respectively. Identical profiles were observed for the by-products production/degradation using the two samples containing Ag₂S as catalysts; these results suggested a more active role of this semiconductor beyond its

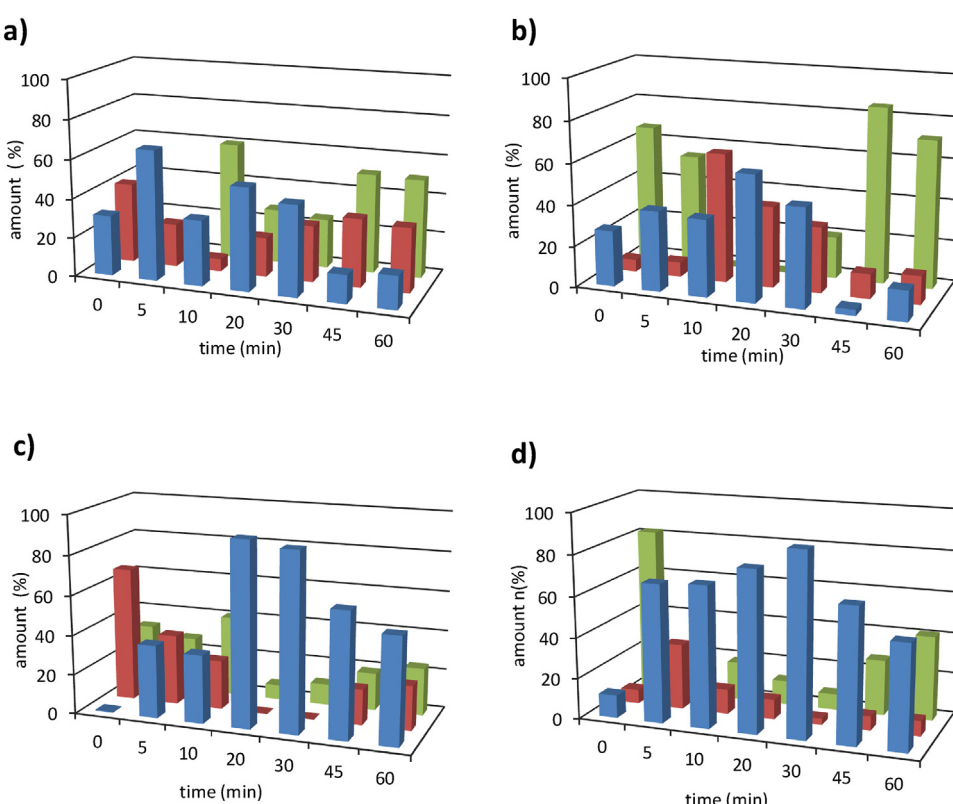


Fig. 8. Concentration profiles of hydroquinone (blue), benzoquinone (red), and catechol and resorcinol mixture (green) for the period of 120 min of irradiation, during photolysis (a), and using TNF (b), Ag₂S/TNF (c), and nanoAg₂S (d) samples as catalysts.

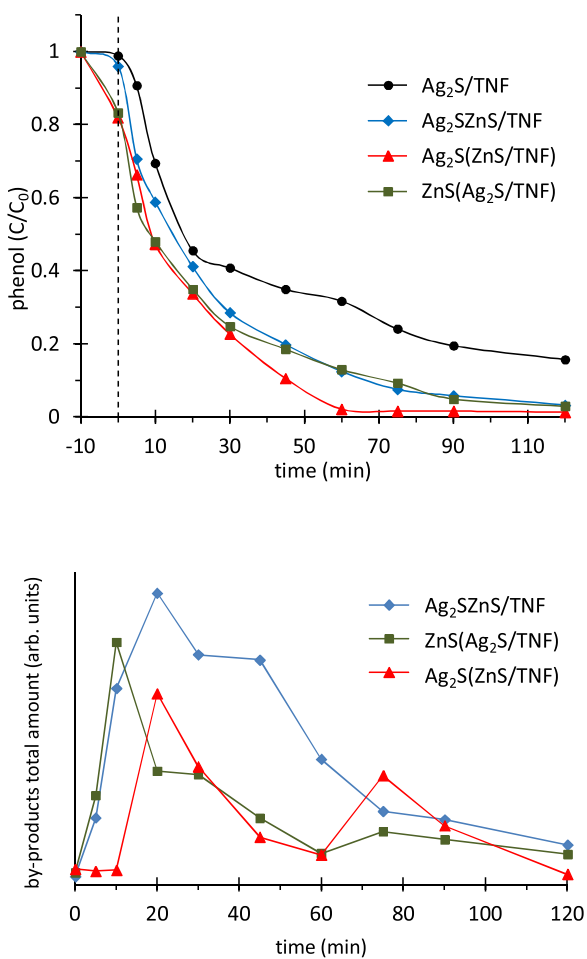


Fig. 9. a) Profiles of phenol photodegradation catalyzed by the co-sensitized TNF samples, over 120 min of irradiation; b) total amount of by-products present in solution during the 120 min of irradiation.

contribution for the increase of nanocomposite's visible radiation absorption.

3.3.2. Using TNF sensitized with $\text{Ag}_2\text{S-ZnS}$

The profiles of phenol photodegradation catalyzed by the co-sensitized TNF samples, over 120 min of irradiation are shown in Fig. 9a. As can be observed, for all the samples, no significant phenol adsorption occurred prior to irradiation and identical degradation profiles were observed for the initial times of reaction. After 60 min of irradiation the best degradation results, with 100% of phenol removal, were obtained using the $\text{Ag}_2\text{S}(\text{ZnS}/\text{TNF})$ sample as catalyst. The photocatalytic performance for the other two samples, $\text{Ag}_2\text{S}\text{ZnS}/\text{TNF}$ and $\text{ZnS}(\text{Ag}_2\text{S}/\text{TNF})$, was identical, with 87% of phenol degradation, after 120 min of irradiation. For these two catalysts a longer time, higher than 120 min was required in order to attain the complete removal of the pollutant. These results were in agreement with the ones obtained for the hydroxyl radical production, reported as the main oxidant species on the phenol photodegradation processes [42].

Using the best photocatalytic sample, $\text{Ag}_2\text{S}(\text{ZnS}/\text{TNF})$ the reusability ability and stability of these powders were checked. After 4 cycles of irradiation, 60 min each, the degree of phenol was kept at 100%, showing no loss of catalytic activity of the sample during these tests. The XRD pattern of this sample, performed after irradiation evidenced no changes in the structure (Fig. S3).

In these processes, the assessment to by-products formation and degradation is also a concern to be aware of. These results allowed

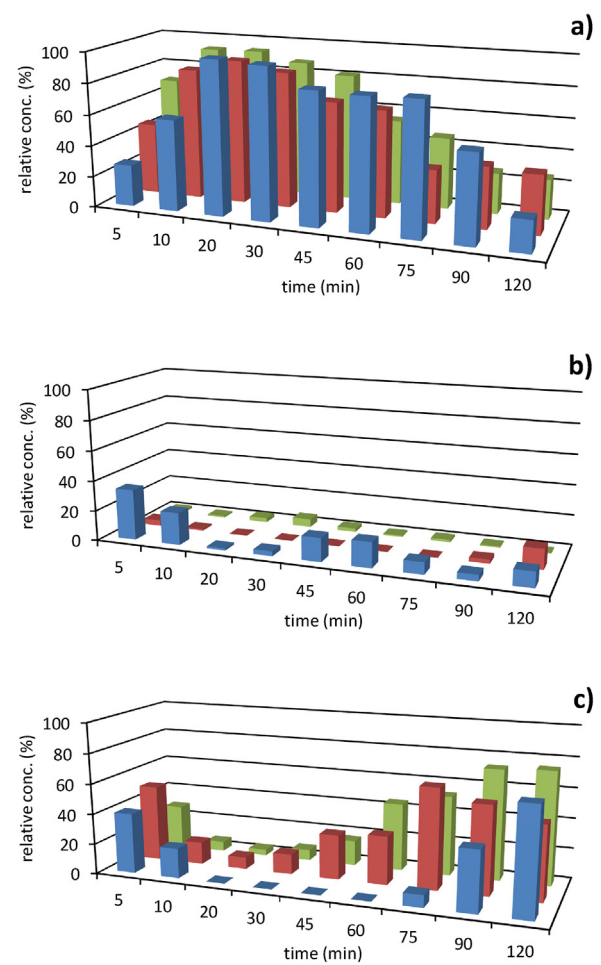


Fig. 10. Amount of the phenol photodegradation by-products, hydroquinone (a), benzoquinone (b) and catechol and resorcinol mixture (c) during 120 of irradiation, using the co-sensitized samples, $\text{Ag}_2\text{S}(\text{ZnS}/\text{TNF})$ (blue), $\text{ZnS}(\text{Ag}_2\text{S}/\text{TNF})$ (red), and $\text{Ag}_2\text{S}\text{ZnS}/\text{TNF}$ (green) as catalysts.

us to better understand the degradation pathways and to avoid the formation of more toxic products than phenol itself. In this case, and supported by bibliography [42,43] benzoquinone, hydroquinone, and catechol and resorcinol mixture were considered by-products and were monitored during 120 min of irradiation. Fig. 9b shows the amount of these compounds formed during phenol photocatalytic degradation reactions. As can be seen, the highest amount of products was observed at 10 min, using the $\text{ZnS}(\text{Ag}_2\text{S}/\text{TNF})$ sample, and at 20 min for the others two catalysts. It is worth of notice that for a time longer than 60 min and using the $\text{Ag}_2\text{S}(\text{ZnS}/\text{TNF})$ catalyst, the corresponding profile in Fig. 9b, and since no phenol was detected after this time (Fig. 9a), could only be attributed to a parallel process of the by-products photodegradation. From these results analysis, it could be concluded that after 120 min of irradiation, the catalyst that produced the lower amount of secondary products was also the $\text{Ag}_2\text{S}(\text{ZnS}/\text{TNF})$ sample.

The identification of the products obtained during each catalytic phenol photodegradation run was carried out; Fig. 10 illustrates the effect of the catalyst used. Hydroquinone was the compound with the highest production, for all the nanocomposites tested, during the 120 min of irradiation. For times of irradiation longer than 60 min, the mixture of catechol and resorcinol was detected as degradation products of the $\text{Ag}_2\text{S}(\text{ZnS}/\text{TNF})$, $\text{ZnS}(\text{Ag}_2\text{S}/\text{TNF})$ and $\text{Ag}_2\text{S}\text{ZnS}/\text{TNF}$, catalyzed processes. In all the three cases, the appearance of such mixture was more notorious for longer periods of irradiation.

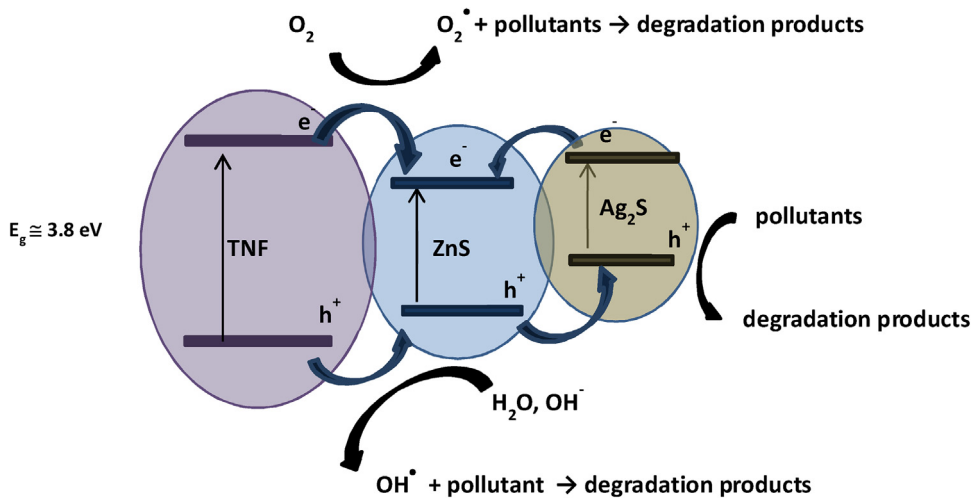


Fig. 11. Band structure scheme of $\text{Ag}_2\text{S}(\text{ZnS}/\text{TNF})$ particles and mechanism of photocatalytic degradation of phenol.

It was interesting to note that using the $\text{Ag}_2\text{S}\text{ZnS}/\text{TNF}$ sample, the existence of benzoquinone as by-product of phenol degradation was very reduced, during irradiation. This effect was also visible for the other two nanocomposites but for these cases a slighter increase on benzoquinone concentrations with time was visible. For all the catalysts, after a high production of hydroquinone, with a maximum at around 20 min, a slow decrease of such compound was noticed. It was interesting that this time (20 min) corresponded also to minima of catechol and resorcinol amounts. A simultaneous analysis of Fig. 10a and c seems to support the idea that hydroquinone was catalytically converted into catechol and/or resorcinol.

Based on the obtained results, a mechanism for the main charge-transfer process in the irradiated catalyst, between TNF, ZnS and Ag_2S nanoparticles, after activation by the light and in the presence

of phenol as model pollutant, is proposed in Fig. 11. After irradiation of an aqueous $\text{Ag}_2\text{S}(\text{ZnS}/\text{TNF})$ suspension with energy higher than its bandgap, electrons (e^-) and holes (h^+) are generated in the conduction (CB) and valence bands (VB), respectively. Due to the relative energetic positions of TNF, ZnS and Ag_2S valence bands, part of the holes generated in TNF and ZnS particles will react with OH^- or H_2O oxidizing them to OH^\bullet radicals [28]. Some of the h^+ will be energetically transferred to the VB of Ag_2S , that here acts as holes scavenger, promoting carrier separation. Ag_2S surface will also act as catalytic sites for phenol oxidation. Simultaneously, some of the e^- from Ag_2S and TNF conduction bands will be transferred to ZnS, enhancing the separation of electrons and holes and reducing the recombination rate. The combined action of h^+ and other highly oxidant species formed during the process will be responsible for phenol mineralization.

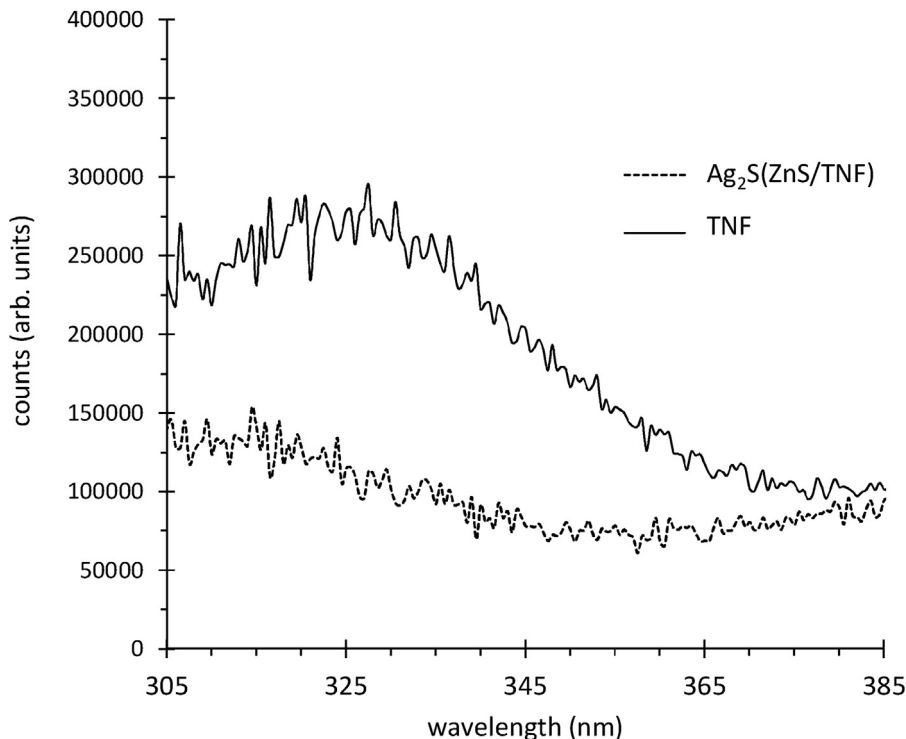


Fig. 12. PL spectra of the TNF and $\text{Ag}_2\text{S}(\text{ZnS}/\text{TNF})$ particles (with excitation at 286 nm).

To confirm the recombination rate reduction due to the synergistic combination of ZnS and Ag₂S nanoparticles, the photoluminescence (PL) spectra of the TNF and Ag₂S(ZnS/TNF) samples were recorded (Fig. 12) for the peak at 330 nm that was attributed to the band-to-band transitions (bandgap transition) [44]. The decrease observed in the PL peak intensity, for the Ag₂S(ZnS/TNF) sample when compared with TNF, could be related with a higher and more efficient electron-hole separation and consequently with a lower recombination rate.

4. Conclusions

The synthesis of novel nanomaterials combining TNF with Ag₂S nanocrystallites was successfully achieved. The Ag₂S nanoparticles were grown onto the TNF's surface through a single-source precursor methodology. Aiming to enhance the Ag₂S/TNF photocatalytic performance, the combination with ZnS nanocrystallites was accomplished using either a co-sensitization or a layer-by-layer approach. TNF nanocomposites with different Ag₂S-ZnS layouts were obtained. The photocatalytic activity of the prepared powders was evaluated throughout the production of the OH[•] radical, presenting the nanoAg₂S sample the best performance for this reaction. The photocatalytic activity of the Ag₂S-ZnS/TNF samples was investigated using phenol as model pollutant and the results indicated that the best results, concerning the time for phenol removal, were obtained using the sample Ag₂S(ZnS/TNF). The identification and quantification of the main by-products suggested distinct mechanisms for the photocatalytic degradation of phenol.

Based on the results obtained, mechanisms for the catalytic nanoAg₂S, Ag₂S/TNF and Ag₂S(ZnS/TNF) actuation, under irradiation, comprising the active role of the Ag₂S nanoparticles in the processes were proposed.

Acknowledgement

The authors thank Fundação para a Ciência e Tecnologia for financial support (UID/MULTI/00612/2013, PEst-OE/QUI/UI0612/2013, SFRH/BD/101220/2014 and IF/01210/2014).

Appendix A. Supplementary data

Supplementary data associated with this article can be found, in the online version, at <http://dx.doi.org/10.1016/j.apcatb.2017.06.089>.

References

- [1] Photocatalysis: science and technology, in: M. Kaneko, I. Okura (Eds.), *Biol. Med. Phys. Series*, Springer, Berlin, 2010.
- [2] A.L. Linsebigler, G. Lu, J.T. Yates Jr., Photocatalysis on TiO_n surfaces: principles, mechanisms, and selected results, *Chem. Rev.* 95 (1995) 735–758.
- [3] D.V. Bavykin, F.C. Walsh, *Titanate and Titania Nanotubes: Synthesis, Properties and Applications*, Cambridge, Royal Society of Chemistry, UK, 2010.
- [4] D.V. Bavykin, J.M. Friedrich, F.C. Walsh, Protonated titanates and TiO₂ nanostructured materials: synthesis, properties, and applications, *Adv. Mater.* 18 (2006) 2807–2824.
- [5] S. Lu, H. Zhong, D. Mo, Z. Hu, H. Zhou, Y. Yao, A H-titanate nanotube with superior oxidative desulfurization selectivity, *Green Chem.* 9 (2017) 1371–1377.
- [6] A. Chen, T. Zhao, H. Gao, L. Chen, J. Chen, Y. Yu, Titanate nanotube-promoted chemical fixation of carbon dioxide to cyclic carbonate: a combined experimental and computational study, *Catal. Sci. Technol.* 78 (2016) 780–790.
- [7] V. Bem, M.C. Neves, M.R. Nunes, A.J. Silvestre, O.C. Monteiro, Influence of the sodium/proton replacement on the structural, morphological and photocatalytic properties of titanate nanotubes, *J. Photochem. Photobiol. A* 232 (2012) 50–56.
- [8] T.A. Silva, J. Diniz, L. Paixão, B. Vieira, B. Barrocas, C.D. Nunes, O.C. Monteiro, Novel titanate nanotubes-cyanocobalamin materials: synthesis and enhanced photocatalytic properties for pollutants removal, *Solid State Sci.* 63 (2017) 30–41.
- [9] A. Papa, J. Boudon, V. Bellat, A. Loiseau, H. Bisht, F. Sallem, R. Chassagnon, V. Bérard, N. Millot, Dispersion of titanate nanotubes for nanomedicine: comparison of PEI and PEG nanohybrids, *Dalton Trans.* 24 (2015) 739–746.
- [10] Q. Wang, J. Huang, H. Li, Z. Chen, A. Zhao, Y. Wang, K. Zhang, H. Sun, S.S. Al-Deyab, Y. Lai, TiO₂ nanotube platforms for smart drug delivery: a review, *Int. J. Nanomed.* 11 (2016) 4819–4834.
- [11] J. Hu, S. Hu, Y. Yang, S. Tong, J. Cheng, M. Chen, L. Zhao, J. Duan, Influence of anodization time on photovoltaic performance of DSSCs based on TiO₂ nanotube array, *Int. J. Photoenergy* 2016 (2016) 4651654–4651661.
- [12] J. Hu, S. Hu, Y. Yang, S. Tong, J. Cheng, M. Chen, L. Zhao, J. Duan, Influence of anodization time on photovoltaic performance of DSSCs based on TiO₂ nanotube array, *Int. J. Photoenergy* 2016 (2016) 4651654–4651661.
- [13] S. Park, S. Kim, S. Park, W.I. Lee, C. Lee, Effects of functionalization of TiO₂ nanotube array sensors with Pd nanoparticles on their selectivity, *Sensors* 14 (2014) 15849–15860.
- [14] J.F. Cabrita, V.C. Ferreira, O.C. Monteiro, Titanate nanofibers sensitized with nanocrystalline Bi₂S₃ as new electrocatalytic materials for ascorbic acid sensor applications, *Electrochim. Acta* 135 (2014) 121–127.
- [15] S. Feizpoor, A. Habibi-Yangjeh, S. Vadivel, Novel TiO₂/Ag₂CrO₄ nanocomposites: efficient visible-light-driven photocatalysts with n-n heterojunctions, *J. Photochem. Photobiol. A* 341 (2017) 57–68.
- [16] M. Pirhashemi, A. Habibi-Yangjeh, Ultrasonic-assisted preparation of plasmonic ZnO/Ag/Ag₂WO₄ nanocomposites with high visible-light photocatalytic performance for degradation of organic pollutants, *J. Colloid Interf. Sci.* 491 (2017) 216–229.
- [17] M. Shekofteh-Gohari, A. Habibi-Yangjeh, Fe₃O₄/ZnO/CoWO₄ nanocomposites: novel magnetically separable visible light-driven photocatalysts with enhanced activity in degradation of different dye pollutants, *Ceram. Int.* 43 (2017) 3063–3071.
- [18] T.J. Entradas, J.F. Cabrita, B. Barrocas, M.R. Nunes, A.J. Silvestre, O.C. Monteiro, Synthesis of titanate nanofibers co-sensitized with ZnS and Bi₂S₃ nanocrystallites and their application on pollutants removal, *Mater. Res. Bull.* 72 (2015) 20–28.
- [19] Z. Pan, X. Zhong, A ZnS and metal hydroxide composite passivation layer for recombination control in high efficiency quantum dot sensitized solar cells, *J. Mater. Chem. A* 4 (2016) 18976–18982.
- [20] W. Jiang, Z. Wu, X. Yue, S. Yuan, H. Lu, B. Liang, Photocatalytic performance of Ag₂S under irradiation with visible and near-infrared light and its mechanism of degradation, *RSC Adv.* 5 (2015) 24064–24071.
- [21] S.K. Yadav, P. Jeevanandam, Synthesis of Ag₂S-TiO₂ nanocomposites and their catalytic activity towards rhodamine B photodegradation, *J. Alloys Compd.* 649 (2015) 483–490.
- [22] W. Hu, L. Zhao, Y. Zhang, X. Zhang, L. Dong, S. Wang, Y. He, Preparation and photocatalytic activity of graphene modified Ag₂S composite, *J. Exp. Nanosci.* 11 (2016) 433–444.
- [23] S. Yue, B. Wei, X. Guo, S. Yang, L. Wang, J. He, Novel Ag₂S/ZnS/carbon nanofiber ternary nanocomposite for highly efficient photocatalytic hydrogen production, *Catal. Comm.* 76 (2016) 37–41.
- [24] X. Cheng, Q. Cheng, X. Deng, P. Wang, H. Liu, Construction of TiO₂ nano-tubes arrays coupled with Ag₂S nano-crystallites photoelectrode and its enhanced visible light photocatalytic performance and mechanism, *Electrochim. Acta* 184 (2015) 264–275.
- [25] J. Hu, L. Ren, Y. Guo, H. Liang, A. Cao, L. Wan, C. Bai, Mass production and high photocatalytic activity of ZnS nanoporous nanoparticles, *Angew. Chem. Int. Ed.* 44 (2005) 1269–1273.
- [26] G. Wang, B. Huang, Z. Li, Z. Lou, Z. Wang, Y. Dai, M. Whangbo, Synthesis and characterization of ZnS with controlled amount of S vacancies for photocatalytic H₂ production under visible light, *Sci. Rep.* 5 (2015) 8544, <http://dx.doi.org/10.1038/srep08544>.
- [27] X. Zhang, X. Liu, L. Zhang, D. Li, S. Liu, Novel porous Ag₂S/ZnS composite nanospheres: fabrication and enhanced visible-light photocatalytic activities, *J. Alloys Compd.* 655 (2016) 38–43.
- [28] X. Yang, H. Xue, J. Xu, X. Huang, J. Zhang, Y. Tang, T. Ng, H. Kwong, X. Meng, C. Lee, Synthesis of porous ZnS:Ag₂S nanosheets by ion exchange for photocatalytic H₂ generation, *ACS Appl. Mater. Interfaces* 6 (2014) 9078–9084.
- [29] H. Zhang, B. Wei, L. Zhu, J. Yu, W. Sun, L. Xu, Applied cation exchange synthesis of ZnS-Ag₂S microspheric composites with enhanced photocatalytic activity, *Surf. Sci.* 270 (2013) 133–138.
- [30] Y. Xie, S.H. Heo, Y.N. Kim, S.H. Yoo, S.O. Cho, Synthesis and visible-light-induced catalytic activity of Ag₂S-coupled TiO₂ nanoparticles and nanowires, *Nanotechnology* 21 (2010) 015703–015710.
- [31] I. Kornarakis, I.N. Lykakis, N. Vordos, G.S. Armatas, Efficient visible-light photocatalytic activity by band alignment in mesoporous ternary polyoxometalate–Ag₂S–CdS semiconductors, *Nanoscale* 6 (2014) 8694–8703.
- [32] R. Zamiri, H.A. Ahangar, D.M. Tobaldi, A. Rebelo, M.P. Seabra, M. Shabani, J.M.F. Ferreira, Fabricating and characterising ZnO–ZnS–Ag₂S ternary nanostructures with efficient solar-light photocatalytic activity, *Phys. Chem. Chem. Phys.* 16 (2014) 22418–22425.
- [33] E.K. Ylhainen, M.R. Nunes, A.J. Silvestre, O.C. Monteiro, Synthesis of titanate nanostructures using amorphous precursor material and their adsorption/photocatalytic properties, *J. Mater. Sci.* 47 (2012) 4305–4312.
- [34] O.C. Monteiro, M.C. Neves, T. Trindade, Submicron silica nanocoating with zinc sulfide using a single source method, *J. Nanosci. Nanotechnol.* 4 (2004) 146–150.

[35] G. Naudin, T. Entradas, B. Barrocas, O.C. Monteiro, Titanate nanorods modified with nanocrystalline ZnS particles and their photocatalytic activity on pollutant removal, *J. Mater. Sci. Technol.* 32 (2016) 1122–1128.

[36] G. Kortuem, Reflectance Spectroscopy: Principles, Methods and Applications, Springer-Verlag, New York, 1969.

[37] K. Krumova, G. Cosa, Singlet oxygen applications in biosciences and nanosciences, in: S. Nonell, C. Flors (Eds.), Book Series: Comprehensive Series in Photochemical & Photobiological Sciences, vol. 1, Royal Society of Chemistry, UK, 2016.

[38] Y. Xu, M.A.A. Schoonen, The absolute energy positions of conduction and valence bands of selected semiconducting minerals, *Am. Mineral.* 85 (2000) 543–556.

[39] R.G. Pearson, Absolute electronegativity and hardness application to inorganic chemistry, *Inorg. Chem.* 27 (1988) 734–740.

[40] A. Akhundi, A. Habibi-Yangjeh, Facile preparation of novel quaternary $g\text{-C}_3\text{N}_4/\text{Fe}_3\text{O}_4/\text{AgI}/\text{Bi}_2\text{S}_3$ nanocomposites: magnetically separable visible-light-driven photocatalysts with significantly enhanced activity, *RSC Adv.* 6 (2016) 106572–106583.

[41] A. Akhundi, A. Habibi-Yangjeh, Novel $g\text{-C}_3\text{N}_4/\text{Ag}_2\text{SO}_4$ nanocomposites: fast microwave-assisted preparation and enhanced photocatalytic performance towards degradation of organic pollutants under visible light, *J. Colloid Interf. Sci.* 482 (2016) 165–174.

[42] E. Grabowska, J. Reszczynska, A. Zaleska, Mechanism of phenol photodegradation in the presence of pure and modified-TiO₂: a review, *Water Res.* 46 (2012) 5453–5471.

[43] M.C. Neves, J.M.F. Nogueira, T. Trindade, M.H. Mendonça, M.I. Pereira, O.C. Monteiro, Photosensitization of TiO₂ by Ag₂S and its catalytic activity on phenol photodegradation, *J. Photochem. Photobiol. A* 204 (2009) 168–173.

[44] N. Pugazhenthiran, S. Murugesan, S. Anandan, High surface area Ag-TiO₂ nanotubes for solar/visible-lightphotocatalytic degradation of ceftiofur sodium, *J. Hazard. Mater.* 263 (2013) 541–549.